
Investigation of Laser-Induced Damage in Hafnia/Silica Multilayer Dielectric Coatings Under 1053-nm, 600-fs to 100-ps Laser Irradiation

Introduction

The limiting factor governing the output power in current-generation, large-aperture laser systems^{1,2} is typically related to the resistance of its optical components to laser-induced damage.^{3,4} The energy coupling is facilitated by the presence of defects related to fabrication-specific processes and operational environment-related parameters. The mechanisms of damage initiation with nanosecond pulses and associated material modification have been extensively studied in recent years. However, the processes involved in laser damage for pulse durations between about 0.5 and 100 ps remain poorly understood. Our research efforts have been focused on this intermediate temporal regime and are motivated by the need to improve the damage-performance characteristics and reduce the cost of operations of the OMEGA EP Laser System, operating at 1053-nm wavelength and with an adjustable pulse duration between 0.7 and 100 ps.

The morphology of the damage sites is governed by (a) the location of energy deposition; (b) the laser parameters (such as pulse length, spatial characteristics of the beam, and wavelength); and (c) the material thermodynamic properties that determine the material relaxation following laser-energy coupling and deposition. Consequently, the morphology of the damage sites provides signatures of the thermodynamic pathway of laser damage that can aid in understanding the origin and evolution of damage. This information, in turn, can be used for designing and fabricating next-generation optical components with higher damage thresholds.

Multilayer dielectric (MLD) coatings are widely used in large-aperture, short-pulse laser systems. MLD coatings typically involve alternating high- and low-refractive-index layers, where laser-induced damage can initiate in different layers within the MLD stack. The focus of the present work is to provide a more-detailed description of the damage morphology in MLD-coated high reflectors and to identify the underlying damage-initiation mechanism. Specifically, we investigate low-loss MLD SiO₂/HfO₂ mirrors that were fabricated at LLE in order to have a precise knowledge of the design and, conse-

quently, the associated standing-wave electric-field intensities within the layer structure. Detailed imaging of the damage sites, typically obtained with scanning electron microscopy (SEM) and atomic force microscopy (AFM), is used to characterize their morphologies and directly correlate to the location of energy deposition and the corresponding electric-field distribution. The depth measurements are used as a diagnostic to identify the location of the initial energy deposition within the MLD stack. The results suggest that there are three distinct damage-initiation morphologies: the first prevailing at laser pulse lengths shorter than about 2.3 ps, while the other two are observed for longer pulses. Modeling of the processes involved for each type of damage morphology helps reveal the underlying mechanism of laser-induced damage.

Experimental Details

The laser system used in this study operates at 1053 nm with an adjustable pulse duration between 600 fs and 100 ps. The laser beam is focused on the sample using a 200-cm-focal-length mirror providing a nearly circular, ~350- μ m-diam beam spot. Each tested site on the sample is exposed to a single pulse at a predetermined fluence in a vacuum chamber at a pressure of $\sim 10^{-6}$ Torr. Various samples representing typical SiO₂/HfO₂ MLD mirror designs fabricated via electron-beam deposition were used in this study. The distribution of electric-field intensity within the MLD stack was calculated using commercially available software (OptiLayer).

Experimental Results

The results suggest that there are three general morphologies of damage sites observed with characteristic examples as shown in Figs. 155.42–155.44. These damage morphologies (denoted as type I, type II, and type III) are observed at different laser pulse durations, with type I observed for pulses between 0.6 ps (lower limit of our laser pulse tunability) and 2.3 ps, and types II and III observed for pulses between 2.3 ps and 100 ps (upper limit of our laser pulse tunability). The images in Fig. 155.42 demonstrate the key characteristics of type-I damage sites. Their morphology involves large shallow craters having a diameter of the order of 30 μ m, which corresponds to the diameter of the laser impinging

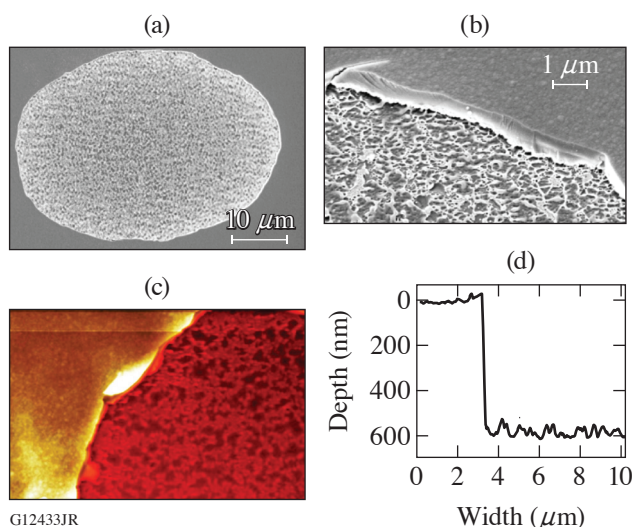


Figure 155.42 [(a),(b)] Scanning electron microscopy (SEM) and (c) atomic force microscopy (AFM) images of type-I damage sites. (d) AFM image cross section data make it possible to evaluate the crater depth and roughness.

on the sample having intensity above the damage threshold. The general morphology of a type-I damage site is best captured by the lower-resolution SEM image shown in Fig. 155.42(a). Typical characteristics include well-defined edges and a quasi-circular profile (affected by the beam shape and beam-incidence angle) that is centered at the location of peak intensity within the laser beam. The sidewalls are nearly vertical, while the bottom of the crater is rough, possibly associated with melted material remnants formed during the damage process. These features are captured in the higher-resolution SEM image shown in Fig. 155.43(b) and the AFM image shown in Fig. 155.43(c). The associated cross sections of AFM images [example shown in Fig. 155.43(d)] allow the depth of the crater to be measured, which is expected to be directly related to the depth of energy deposition (damage initiation and plasma formation). The roughness at the bottom of the crater can also be quantified and is found to typically be of the order of 50 nm (peak to valley). Depending on the coating design as well as the angle and polarization of incident light, the bottom of the crater is located either within the top SiO_2 layer or at the interface between the first HfO_2 and the second SiO_2 layer. Comparison with the calculated electric-field distribution within the stack reveals that these positions correspond to a depth of the first or second electric-field-intensity (EFI) peak, respectively. The observed depths correlate very precisely (within less than 10 nm) to the location of damage initiation as predicted by the electric-field-limited model.⁵

Figure 155.43 captures the typical morphology of the second type of damage site (type II) observed under excitation with

pulses longer than ~ 2.5 ps. Type-II damage sites are isolated, indicating that they originate from nanoscale defects. The diameter of these sites is of the order of a few hundred nanometers to a few micrometers, largely dependent on the laser pulse duration. The images of damage sites shown in Fig. 155.43 were generated at different pulse lengths, characterizing the damage in great detail. All SEM images shown in Fig. 155.43 are on the same spatial scale so that one can compare the change in morphology as a function of pulse duration. Specifically, Figs. 155.43(a)–155.43(d) show damage sites formed under irradiation with 4.6-, 10-, 20-, and 100-ps pulses, respectively. In general, the size of type-II damage sites is found to be proportional to the pulse length of the laser illumination.

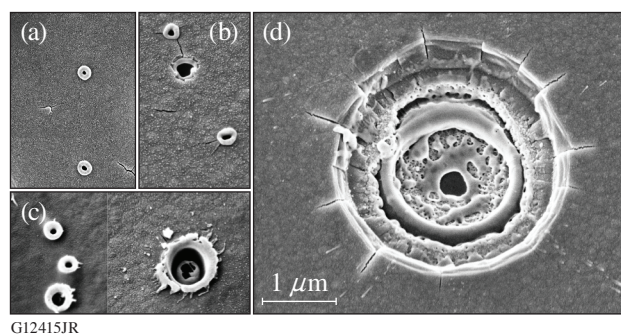


Figure 155.43 SEM images of type-II damage sites formed under exposure to 1064-nm, (a) 4.6-, (b) 10-, (c) 20-, and (d) 100-ps laser pulses.

The complex crater morphology contains a venting hole and one or more inner quasi-spherical shells. This elaborate structure is accompanied by the remnants of melted material, indicating a slow cooling process after the energy is deposited. In addition, the craters are surrounded by radial cracks of the order of $0.5 \mu\text{m}$ to $1 \mu\text{m}$ in length, indicating the presence of tensile hoop stresses surrounding the crater region. Frequently, some of the sites can be characterized by a set of concentric radial cracks with no well-defined venting holes [see examples in Fig. 155.43(a)]. AFM images indicate that the damage is initiated at locations of peak electric-field intensity near the first hafnia-silica interface. These features suggest that damage-precursor defects are located deep within the MLD structure, while damage initiates at sites of localized peak electric-field intensity.

Type-III damage morphology sites were also observed for pulse durations longer than ~ 2.3 ps, consisting of isolated shallow craters having a diameter of ~ 2 to $3 \mu\text{m}$ and a depth smaller than about 150 nm. Figure 155.44(a) shows a Nomar-

ski microscope image of an area exposed to a single 10-ps pulse that generated both type-II and type-III damage sites, which appear as darker and brighter features, respectively. The type-III damage sites extend further from the center of the beam, indicating that their damage threshold is lower. Figures 155.44(b) and 155.44(c) show representative AFM and SEM images. Cross-section data obtained from AFM images reveal that type-III damage sites consist of quasi-conical pits. Higher-magnification SEM images from the middle (bottom) of the pit (see inset) reveal the presence of multiple features having diameters of the order of 10 nm. These features might be the signature of the material modification following plasma formation by damage-initiating defects located at the bottom of the pit having diameters of the order of 50 nm or less. It is important to note that the depth of type-III damage sites is not correlated with the electric-field-intensity peak, in contrast with observations for type-I and type-II damage sites.

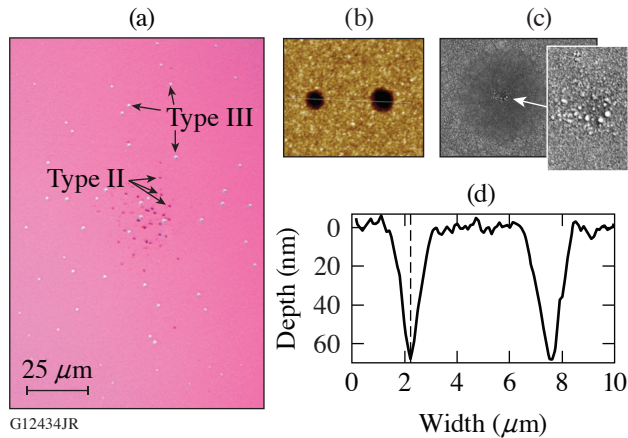


Figure 155.44

(a) Nomarski microscope image of a damage site generated with 10-ps pulses containing both type-II and -III damage sites. (b) AFM and (c) SEM of type-II damage sites. The inset shows the center of the damage site with higher magnification. (d) AFM image cross section data capture the spatial profile of the type-III damage sites.

Modeling

To better understand the mechanisms associated with the experimentally observed damage morphologies, we explore micro- and nanomechanical models of the material's response to the generation of high pressure and temperature during laser-energy deposition. The observed morphology is initially used as a guide to develop a qualitative depiction of the processes involved, which is subsequently tested and refined using the modeling tools. The thermomechanical and thermodynamic properties of the constituent silica and hafnia layers of the MLD are governing the dynamic material response. Furthermore,

the mechanical properties of the MLD layers are affected by the microstructure of each layer (and therefore the deposition process), as well as the presence of multiple interfaces.⁶ In this modeling effort we assume a uniaxial yield stress of 4 GPa based on previous work.⁷ For the elastic properties, we assume bulk properties for Young's modulus (72 GPa for silica and 300 GPa for hafnia) and Poisson's ratio (0.17 for silica and 0.25 for hafnia). We also assume bulk values for thermal properties: thermal conductivities of 1 and 2 W/m.K, mass densities of 2200 and 9500 kg/m³, and heat capacities of 750 and 270 J/kg.K for silica and hafnia, respectively. Although the reported values for films can be different from bulk material values,^{8,9} we consider the above values to be a good approximation to explore the development of sensible models of the mechanisms of damage formation in order to interpret the experimental observations.

The damage sites studied in this work were formed at near-damage-threshold conditions. Consequently, the modeling of the three different types of damage sites discussed next is focused on the threshold conditions for initiating damage. As a result, the damage morphology reflects the dominant mechanism involved in the damage-site-formation process.

1. Modeling Mechanism of Type-I Damage Sites

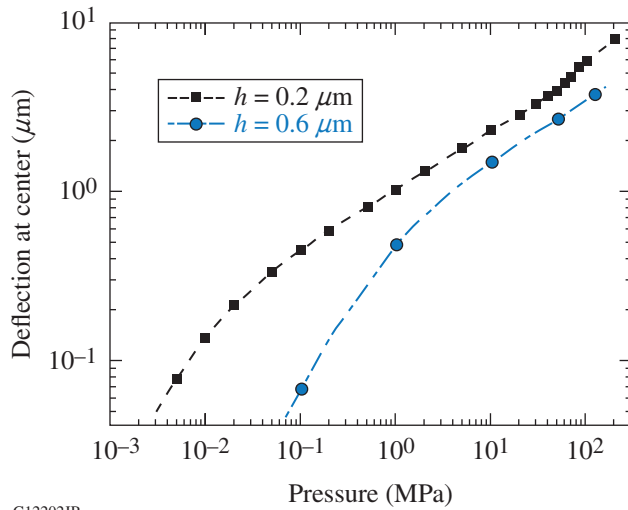
The morphology of a type-I damage site suggests that plasma is initiated within a narrow range of electric-field intensities about the location predicted by the electric-field-limited model. Assuming that this range of electric-field intensity (laterally) is required to support plasma formation (e.g., via multiphoton absorption), we can project the same range of electric-field intensities along the z axis (inside the coating). This enables one to estimate the thickness of the plasma, which is found to be 60 to 80 nm, depending on the irradiation conditions. The observed removal of the overlying layer implies that the generated pressure is sufficient to support its shear fracture and detachment followed by rapid cooling, resulting in remnants of transient liquid material.

Based on the above qualitative description, the model assumes plasma formation within a thin region at depth t_0 below the surface, followed by evaporation and building of a pressure p that induces an inflation of the material above. This, in turn, gives rise to the formation of a circular membrane (blister) having radius a , thickness h (assumed to be the same as the depth of plasma formation from the surface), and center deflection height w_c . The center deflection (w_c) scales with thickness h and material properties as¹⁰

$$(w_c/h) + A(w_c/h)^3 = B(p/e)(a/h)^4, \quad (1)$$

where E is the Young's modulus of the materials while A and B are constants that depend on the Poisson's ratio of the material.

Figure 155.45 shows the center deflection w_c as a function of initial pressure. Calculations were carried out for an array of relevant initial conditions to determine the center deflection w_c as a function of the initial pressure generated by the formed plasma. For example, inflation of an axisymmetric membrane at thickness $h = 200$ nm under pressure $p = 45$ MPa leads to a center deflection $w_c = 3.81$ μm accompanied by the formation of a plastic hinge near the support point of the membrane. For small center deflections, i.e., $w_c \ll h$, w_c scales linearly with pressure $w_c \propto p$ since the material behaves in a linear elastic manner and the strains are small. For larger deflections, i.e., $w_c \gg h$, the scaling is nonlinear and $w_c \propto p^{1/3}$ since the strains (while still elastic) are nonlinear. Furthermore, for small pressures and deflections, the numerical results show that the overall shape of the deflected membrane is well approximated by $w(r) = w_c(1 - r^2/a^2)^2$; i.e., the slope vanishes at the support point. On the other hand, for larger pressures, the shape is essentially spherical and given by $w(r) = w_c(1 - r^2/a^2)$.



G12202JR

Figure 155.45
Model predictions of the center deflection of an inflated membrane for two depths of plasma initiation (membrane thicknesses) of $h = 0.2$ and $h = 0.6$ mm with damage site radius $a = 15$ μm .

The numerical simulations reveal that the stresses at the support point of the inflated membrane always exceed those at the apex; therefore, the failure is expected to initiate at the support point. Although the plastic hinge formation arises at a pressure that scales with the membrane thickness, our numerical simulations indicate that the center deflection is between 3 and 4 μm . On the other hand, the pressure required for the

formation of the hinge scales with the membrane thickness (depth of damage initiation).

2. Modeling Mechanism of Type-II Damage Sites

The morphology of type-II damage sites suggests that a significant amount of melting was generated during the damage process. We therefore assume that the precursor defects (located below the surface) absorb a sufficient amount of energy to form plasma, but the pressure generated cannot support the fracture of the layer above, as in type-I damage sites. As a result, the absorbed energy is dissipated via heat diffusion, ultimately leading to softening of the top layer. The presence of radial cracks surrounding the damage site indicates that the generated gaseous material expands, producing swelling on the surface above the location of energy deposition. This, in turn, generates tensile hoop stresses and cracking of the still-cold top layer. Eventually, a venting path is formed where the gaseous and liquid material is released.

This qualitative description is explored using a thermal model of an absorbing defect located near the bottom of the first hafnia layer, where the defect absorbs the incident laser radiation and rapidly heats up followed by thermal diffusion at the end of the pulse.^{4,11-15} For simplicity we assume that the defect absorbs laser energy proportionally to its cross-sectional area (πR_{defect}^2) and distributes the thermal power over its volume ($(4/3)\pi R_{\text{defect}}^3$), so that the power absorbed per unit volume has a Gaussian temporal dependence:

$$g(t) = g_{\text{max}} \exp\left[-2(t - t_{\text{peak}})/t_{\text{width}}\right]^2, \quad (2)$$

where t_{peak} is the time when the pulse is at its peak intensity and t_{width} is the pulse width.

The maximum value (g_{max}) is given by

$$g_{\text{max}} = (3/2\sqrt{\pi})F/(t_{\text{width}}R_{\text{defect}}), \quad (3)$$

where F is the laser fluence (J/cm^2). Typical trials for our simulations used pulse widths of 10 to 50 ps and $R_{\text{defect}} = 20, 40, \text{ and } 60$ nm with adaptation of the bulk properties for SiO_2 and HfO_2 .

The modeling results shown in Fig. 155.46 were obtained assuming a laser pulse duration and fluence of 50 ps and 15 J/cm^2 , respectively, depicting the temperature distribution resulting from absorption by a defect with a 40-nm radius, 18 ns after illumination. This laser fluence represents the experimentally measured damage threshold in this type of

MLD. The isotherms show that the surface temperature reaches well above the melting point of silica with the heating being asymmetric (higher temperature closer to the surface) because of the presence of the material-free surface where heat diffusion is halted. It must be noted that phase transitions and the temperature-dependent thermomechanical parameters were not considered in the models described above; arguably, it may be impossible with current computational capabilities to take into consideration all essential elements involved. The model provides an adequate description, however, of the key mechanism involved in type-II damage-site formation.

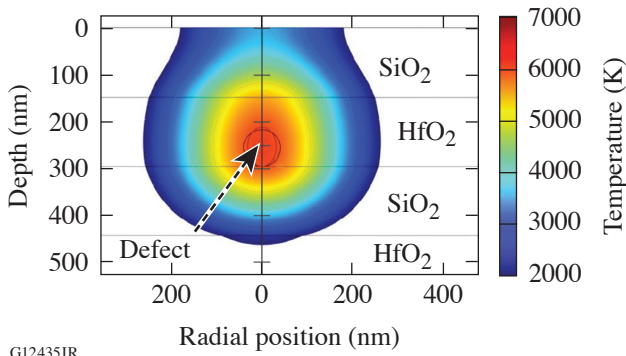


Figure 155.46

Model prediction of the temperature distribution 18 ns after illumination, assuming the defect has a radius of 40 nm and is located at the interface between the second and third layers. The fluence of the incident pulse is 15 J/cm² and the pulse duration is 50 ps.

We attribute the complex morphology of the damage sites to the very different thermodynamic properties of SiO₂ and HfO₂ layers. Specifically, since the melting temperature of the hafnia is very close to the evaporation temperature of the silica, mixed-material phases can be simultaneously present such that heat diffusion can facilitate a melted hafnia layer to be accompanied by evaporation of the adjacent silica layer. As the pressure is released via the formed venting pit, subsequent ejection of hot (potentially a mixture of gas and liquid) material results in rapid cooling. We therefore postulate that the inner shell observed in the damage sites is the hafnia layer involved in the damage process with a venting path for release of the evaporated material of the underlying silica layer.

3. Modeling Mechanism of Type-III Damage Sites

The morphology of type-III damage sites consists of quasi-conical craters with a high aspect ratio and a central-region morphology suggestive of an explosive boiling process. We therefore assume that this type of morphology may be associated with pressure-driven material ejection. Although this

mechanism is similar to that involved in type-I damage sites, the volume of the plasma region depends on the size of the defects and is much smaller than that for type-I damage sites. As a result, the generated pressure energy is much smaller than that for the type-I damage sites. The generated pressure can still be sufficient, however, to remove material above a defect if it is located close to the surface. The AFM imaging results demonstrate that the depth of type-III damage sites is of the order of 150 nm or less, which is consistent with the hypothesis that absorbing defects located close to the surface can give rise to superheating of a small volume and a very localized high pressure.

Based on the above qualitative interpretation, the relevant geometrical parameters considered in modeling are depicted in Fig. 155.47, where the defect is located at a depth h ; i.e., a cone of inclined surface area with α being the cone apex half-angle.

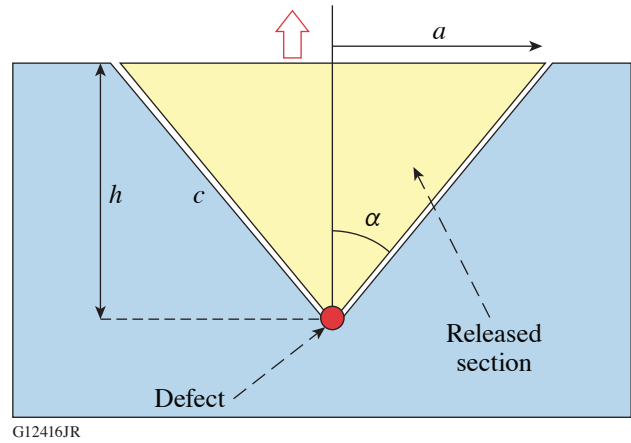


Figure 155.47

Geometrical parameters considered in the modeling of type-III damage sites.

The necessary surface energy is $G_c A_{\text{cone}}$, where G_c is the critical energy-release rate for silica and A_{cone} is the area of the cone representing the newly generated surface. These can be described by

$$A_{\text{cone}} = \pi \alpha (h^2 + a^2)^{1/2} = \pi h^2 / \Omega, \quad \Omega = \cos^2 \alpha / \sin \alpha \quad (4)$$

and

$$G_c = K_c^2 / E_Y, \quad (5)$$

where K_c is the fracture toughness and E_Y is the Young's modulus for silica. The critical energy release rate G_c includes the surface energy and the energy consumed by any irreversible

processes in surface creation (such as plasticity, dislocations, etc.). If the energy released by the superheated defect is E , the resulting crater will reach the surface when

$$E > G_c A_{\text{cone}}, \quad (6)$$

where the energy E absorbed by the defect is $E = F_{\text{th}}(\pi^2 R)$. This leads to a maximum depth h_{max} for the defect where the absorbed energy is sufficient to support the formation of a new surface and create the damage site as given by

$$h_{\text{max}} = R(F_{\text{th}}\Omega/G_c)^{1/2}. \quad (7)$$

The AFM images from Fig. 155.44 show that the angle α is close to 86.5° , leading to $\Omega = 0.004$. Using the value $0.7 \text{ MPa m}^{1/2}$ for the critical stress intensity K_c in fused silica^{16–18} and Young's modulus $E_Y = 70 \text{ GPa}$, the critical energy release rate is $G_c \sim 7 \text{ J/m}^2$. For order-of-magnitude estimates, we use a laser-damage threshold value of $\text{LDT} = 7.5 \text{ J/cm}^2$ yielding

$$h_{\text{max}} = 6.4R. \quad (8)$$

The above approach suggests that the observed maximum depth of $\approx 150 \text{ nm}$ for the type-III damage sites implies that the corresponding maximum radius of the defects is $\approx 24 \text{ nm}$. This approach did not take into account, however, the transient processes that can increase the energy absorbed by the defect site such as absorption by the plasma and plasma expansion during the laser pulse, which would increase the effective radius of the absorbing region. In general, this model utilizes simple energy-balance considerations with reasonable energy-coupling factors. In this manner, it is possible to substantiate that type-III damage sites are superficial and originate from mechanical failure of the overlying material resulting from the energy absorbed by defects located at a maximum depth of the order of 150 nm . We therefore anticipate that such defects, when located deeper in the MLD structure, may create small voids containing melted and densified material without any observable modification on the surface.

Discussion

The damage sites investigated in this work represent the typical morphologies at near-damage-threshold irradiation conditions. It was shown that type-I and type-III damage sites are governed by pressure-induced effects, namely the generation of sufficient pressure to remove an overlying layer of material. On the other hand, type-II damage sites result from heat diffusion, thereby creating a larger amount of melted material and a relatively smaller amount of pressure-induced modifications. In

all cases, however, the generated pressure is the driving mechanism for removing material and/or creating a damage crater.

To generate the required pressure, the material must absorb a sufficient amount of energy to reach evaporation conditions (superheating).¹⁹ The pressure energy generated during the initial phase of the relaxation of the material will inevitably facilitate the formation of a blister or microscale bubble within the material. If this initial pressure-induced modification of the material is not sufficient to cause mechanical failure of the material and subsequent release of the vapor/liquid material (which can be in a superheated state), with a corresponding rapid release of energy, heat generation and diffusion will facilitate the gradual transport of the energy away from the absorbing site. The increase of the temperature of the surrounding material leads to modification of its mechanical properties, which can change the fundamental response of the material. For example, heating can introduce melting of the overlying layer and the formation of a blister that may not erupt. Such formation of unerupted blisters is observed in samples where the damage initiates deeper in the stack or at well above damage-threshold irradiation.

Damage can also be initiated at close proximity so that there is overlap between the affected volumes. For example, we have observed type-II damage sites formed within a distance similar to that of the diameter of the final damage site (of the order of a few microns). In such cases, the combined generated pressure can be sufficient to facilitate mechanical removal of the overlying material generating mixed-type morphologies. In particular, the appearance of side walls indicates that the failure (rupture and creation of a new surface) was from mechanical stress, while there are also visual indications that significant melting was involved. Such damage morphologies are rarely observed (according to our experience) at near-damage-threshold conditions but can be observed at higher fluences.

Damage can be initiated by extrinsic defects such as microscale nodules or flaws in the coating. We have not investigated these cases in the present work. It is expected, however, that the basic principles presented in this work might be applicable. Pressure- and heat-related effects will govern the material response along with field intensification, initiating damage mechanisms similar to that of type-I damage sites. Also, we have not considered the mechanisms of damage growth, which can be considerably different.

Conclusions

This work explores the origins and mechanisms of damage site formation associated with three damage morphologies

observed in SiO₂/HfO₂ multilayer coatings under laser irradiation at 1053 nm with laser pulses from 600 fs to 100 ps in duration. Type-I damage sites are observed for pulses shorter than about 2.5 ps (under the excitation conditions used in this work) and are governed by pressure-induced mechanical ejection of the overlying material following electric-field-induced plasma formation below the surface. Defect-driven damage initiation (type II and type III) is observed for pulse lengths from 2.5 ps to 100 ps. Type-II damage is initiated by defects of the order of 100 nm or less in diameter at a depth defined by the local electric-field-intensity peak. The initial subsurface explosion remains confined and evolves through melting and eventual venting of the evaporated material on a time scale of the order of 20 ns. Type-III damage is associated with the release of material overlying a precursor defect located at depths of less than ≈ 150 nm and shows no correlation with the local electric-field intensity.

ACKNOWLEDGMENT

This material is based upon work supported by the Department of Energy National Nuclear Security Administration under Award Number DE-NA0001944, the University of Rochester, and the New York State Energy Research and Development Authority.

REFERENCES

1. E. Cartlidge, *Science* **359**, 382 (2018).
2. C. Danson *et al.*, *High Power Laser Sci. Eng.* **3**, e3 (2015).
3. L. Gallais, *Proc. SPIE* **9893**, 989305 (2016).
4. A. A. Manenkov, *Proc. SPIE* **53**, 010901 (2014).
5. A. Hervy *et al.*, *Opt. Eng.* **56**, 011001 (2016)
6. K. Mehrotra, J. B. Oliver, and J. C. Lambropoulos, *Appl. Opt.* **54**, 2435 (2015).
7. K. Mehrotra, H. P. Howard, S. D. Jacobs, and J. C. Lambropoulos, *AIP Adv.* **1**, 042179 (2011).
8. J. C. Lambropoulos, M. R. Jolly, C. A. Amsden, S. E. Gilman, M. J. Sinicropi, D. Diakomihalis, and S. D. Jacobs, *J. Appl. Phys.* **66**, 4230 (1989).
9. M. C. Wingert *et al.*, *Semicond. Sci. Technol.* **31**, 113003 (2016).
10. S. Timoshenko and S. Woinowsky-Krieger, *Theory of Plates and Shells*, 2nd ed. (McGraw-Hill, New York, 1987), Sec. 97.
11. B. C. Stuart *et al.*, *J. Opt. Soc. Am. B* **13**, 459 (1996).
12. R. W. Hopper and D. R. Uhlmann, *J. Appl. Phys.* **41**, 4023 (1970).
13. T. H. Walker, A. H. Guenther, and P. Nielsen, *IEEE J. Quantum Electron.* **QE-17**, 2053 (1981).
14. J. Yu *et al.*, *Adv. Cond. Matter Phys.* **2014**, 364627 (2014).
15. R. M. Wood, *Laser-Induced Damage of Optical Materials*, Series in Optics and Optoelectronics (Institute of Physics, Bristol, England, 2003).
16. S. M. Wiederhorn, in *Mechanical and Thermal Properties of Ceramics*, edited by J. B. Wachtman, Jr., NBS Special Publication 303 (National Bureau of Standards, Gaithersburg, MD, 1969), pp. 217–242.
17. M. M. Wood and J. E. Weidlich, *Am. Mineral.* **67**, 1065 (1982).
18. G. Žagar *et al.*, *Scr. Metall.* **112**, 132 (2016).
19. S. G. Demos, R. A. Negres, R. N. Raman, M. D. Feit, K. R. Manes, and A. M. Rubenchik, *Optica* **2**, 765 (2015).